ACS NANO
www.acsnano.org

Single-Layer MoS_2 Grown on Atomically Flat $SrTiO_3$ Single Crystal for Enhanced Trionic Luminescence

Chenxi Huang, Jun Fu, Miaomiao Xiang, Jiefu Zhang, Hualing Zeng,* and Xiang Shao*

Cite This: *ACS Nano* 2021, 15, 8610−8620

Read Online

ABSTRACT: **The elaborate interface interactions can be critical in determining the achievable functionality of a semiconductor heterojunction (SH), particularly when two-dimensional material is enclosed in the system and its thickness is at an atomic extreme. In this work, we have successfully constructed a SH model system composed of typical transition-metal chalcogenide (TMDs) and transition metal oxides (TMO) by directly growing molybdenum sulfide (MoS_2) nanosheets on atomically flat strontium titanate ($SrTiO_3$) single crystal substrates through a conventional chemical vapor deposition (CVD) synthetic method. Multiple measurements have demonstrated the uniform monolayer thickness and single crystallinity of the MoS_2 nanosheets as well as the atomic flatness of the heterojunction surface, both characterizing an extremely high quality of the interface. Clear evidence have been obtained for the electron transfer from the MoS_2 adlayer to the $SrTiO_3$ substrate which varies against the interface conditions. More importantly, the photoluminescence of MoS_2 is significantly tailored, which is correlated with both the cleanness of the interface and the crystal orientation of the $SrTiO_3$ substrate. These results not only shed fresh lights on the structure−property relationship of the TMDs/TMO heterostructures but also manifest the importance of the ideal interface structure for a hybridized system.**

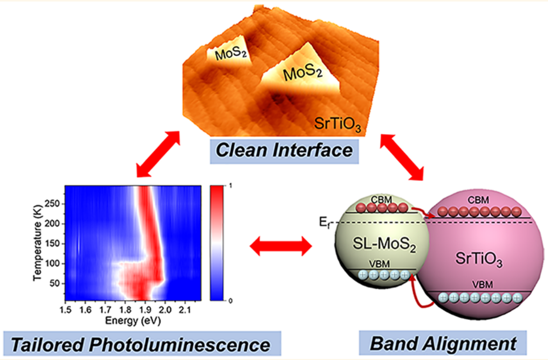

KEYWORDS: *MoS_2, $SrTiO_3$, model system, heterojunction, CVD*

INTRODUCTION

Functionalized semiconductor heterojunctions (FSH) have provoked extensive studies due to their unique physicochemical properties which are interesting for both fundamental science and advanced technology.[1−5] With regard to the synergistic effect of the compositional materials, a sufficiently reasonable and credible interfacial interaction of the FSH can play decisive roles for realizing the anticipated emergent functionalities.[6−10] In the past decade, tremendous studies have been dedicated to achieve creational FSH systems combining variously different semiconductor materials such as FeO_x-TiO_2,[11] CdSe-CdS,[12] ZnS-ZnO,[13] MoS_2-$MoSe_2$,[14] and $LaALO_3$-$SrTiO_3$,[15] which have contributed largely in expanding the material families, fabricating fascinating devices, deepening or renewing the basic understandings of heterogeneous catalysis and condensed matter physics, and so on.[16−18] The fast development in these fields, on the other hand, formulates urgent demands for fundamental studies to unveil the physical natures of these FSH and their corresponding properties, *i.e.*, the structure−property relationships. To this goal, building model systems with atomically precise interfacial structures becomes necessary for the sake of clear interpretations of the various characterization results.

In the extensively explored FSH systems, the two-dimensional materials (2DM) have emerged as an important participator owing to their remarkable properties including the superior conductivity, high chemical stability, conspicuously large surface area, as well as luminescing properties, *etc.*[19−21] The combination of 2DM with transition metal oxides (TMO) frequently constitutes more fascinating heterostructures seeing broad applications in various fields such as solar cells, photoconductors, photodetectors, and so on.[22−24] In such systems, a serious control of the interface structure can be more critical because the properties of the oxides can be

Received: January 18, 2021
Accepted: April 30, 2021
Published: May 5, 2021

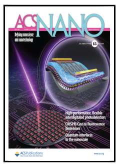

https://doi.org/10.1021/acsnano.1c00482
ACS Nano 2021, 15, 8610−8620

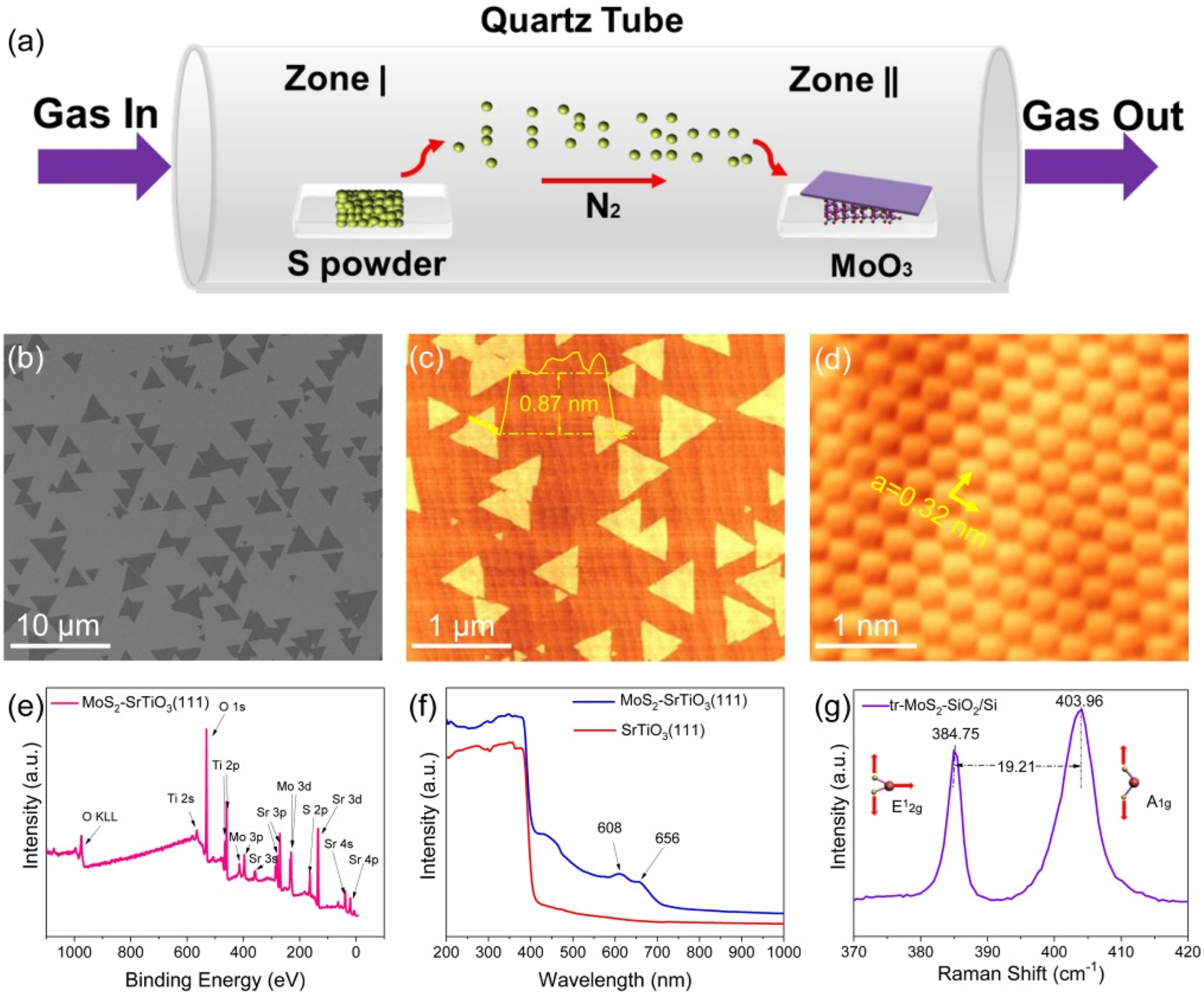

Figure 1. Characterizations of monolayer MoS_2 nanosheets grown on $SrTiO_3(111)$ single crystal surface. (a) Schematic diagram of synthetic process of the MoS_2-$SrTiO_3(111)$ sample. (b) and (c) SEM and AFM images of the MoS_2-$SrTiO_3(111)$ sample, respectively. Inset in (c) shows the height profile of a MoS_2 nanosheet. (d) Atomically resolved STM image measured on a the MoS_2 nanosheet grown on a Nb-doped $SrTiO_3(111)$ substrate. (e) XPS survey spectrum of the MoS_2-$SrTiO_3(111)$ sample showing no clue of unexpected contaminations. (f) UV–vis spectra of the blank $SrTiO_3(111)$ (red) and the MoS_2-$SrTiO_3(111)$ sample (blue), respectively. (g) Raman spectrum of the as-grown MoS_2 nanosheets after transfer onto a SiO_2/Si substrate.

sensitively dependent on their atomic structures and the ad-species, the latter may impose unexpected affections on the overall functionality of the heterostructure. As a representative of these FSH, the compositional system of MoS_2 and $SrTiO_3$ has attracted much interest considering the attractive properties of both materials.[25−40] Particularly, $SrTiO_3$ differs from many other oxides in its distinctive layered structure, high dielectric constant, quantum paraelectricity, *etc.*[41,42] and thus being expected with a special tuning effect over the MoS_2 properties. Recently, S. Sarkar *et al.* discovered a quasiparticle in the MoS_2/$SrTiO_3$ hybridization called "polaronic trion", which is derived from the strong coupling of the soft phonon in $SrTiO_3$ and the negatively charged exciton in MoS_2 at the interface.[27,28] X. Yin and co-workers investigated the same system and discussed the importance of the spin−orbital charge−lattice coupling in tailoring the photo properties of the MoS_2 monolayer.[32] These latest developments undisputedly emphasized the critical roles of the interface interaction between MoS_2 and $SrTiO_3$. However, most of these reports emphasized the quality of the as-grown MoS_2 films yet paid little attention on the $SrTiO_3$ surface structure, which may actually lack the serious control of the MoS_2/$SrTiO_3$ interface.

Here in this work, we have applied a conventional chemical vapor deposition (CVD) method to directly grow high quality MoS_2 nanosheets over $SrTiO_3(111)$ and $SrTiO_3(100)$ single crystal substrates. Our optimized synthetic recipe not only realized the fabrication of single crystallized single-layer MoS_2 (SL-MoS_2) but also ideally preserved the atomic flatness of the $SrTiO_3$ surface, thus successfully constructing ideal MoS_2/$SrTiO_3$ interfaces. The series of surface characterizations clearly confirmed MoS_2 donates electrons to the $SrTiO_3$ substrate, while both materials hold an *n*-type doped nature. Concomitantly, the variable temperature photoluminescence spectroscopy (PL) evidenced a strong tuning effect of the $SrTiO_3$ substrate over the MoS_2 adlayer by significantly enhancing the trion luminescence of the latter. Moreover, such an effect was found seriously dependent on the substrate

https://doi.org/10.1021/acsnano.1c00482
ACS Nano 2021, 15, 8610−8620

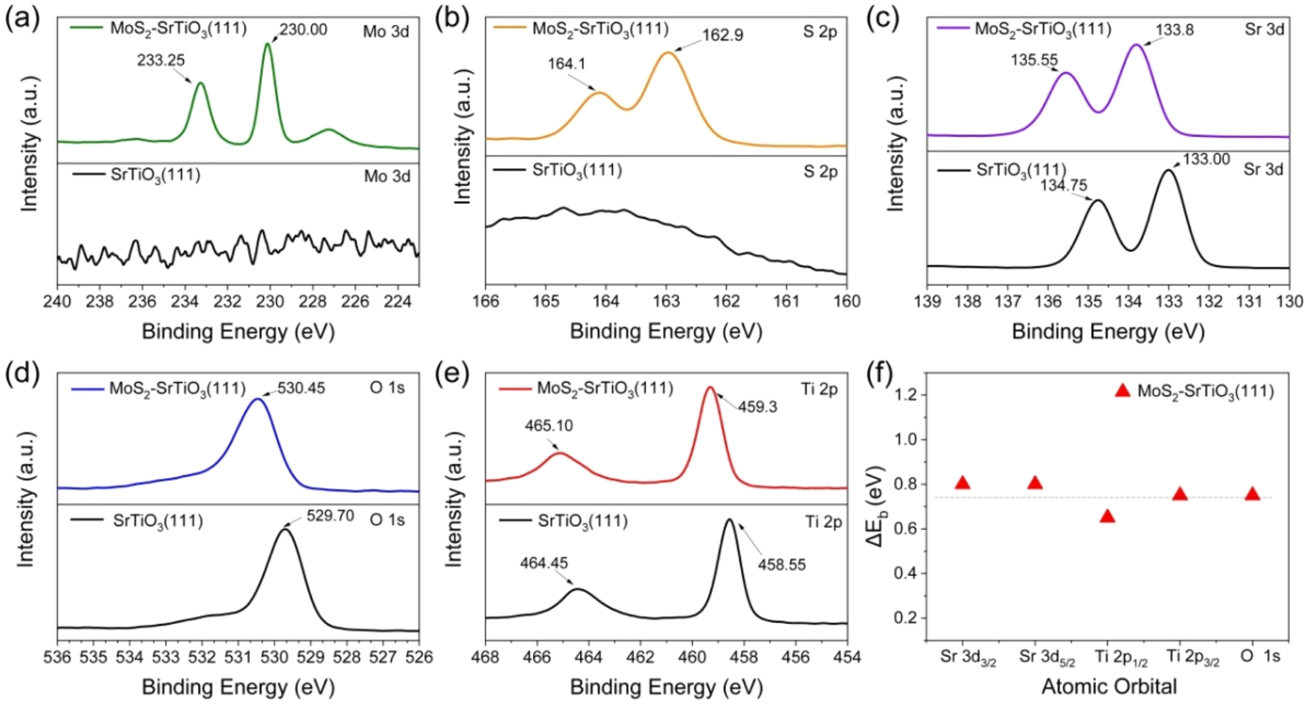

Figure 2. High resolution XPS spectra of (a) Mo 3*d*, (b) S 2*p*, (c) Sr 3*d*, (d) O 1*s*, and (e) Ti 2*p* collected on the blank $SrTiO_3(111)$ substrate and the MoS_2-$SrTiO_3(111)$ sample, respectively. (f) Shifts of the binding energies for Sr, Ti, and O atomic orbitals in the MoS_2-$SrTiO_3(111)$ sample as compared with blank $SrTiO_3(111)$ substrate.

orientation and can be exterminated upon intercalating molecules into the interface region.

RESULTS AND DISCUSSION

Characterization of the As-prepared SL-MoS_2 Nanosheets on $SrTiO_3$. Figure 1 shows a series of characterizations of the as-grown SL-MoS_2 nanosheets on $SrTiO_3(111)$ substrate (termed as MoS_2-$SrTiO_3(111)$). The schematic CVD setup of the two-zone oven is presented in Figure 1a, wherein the prepared $SrTiO_3(111)$ substrate is placed right above the MoO_3 source at the downstream position while the S source is placed on the upstream position and transported by the N_2 carrier with low flow rate. Note that before being subjected to the CVD synthesis of MoS_2, the $SrTiO_3(111)$ substrate has been treated (see the Experimental Section for details) to achieve a clean and atomically flat surface. As shown by the atomic force microscopy (AFM) images in Supporting Information (SI), Figure S1, the treated substrate exhibits large and contamination-free terraces separated by atomic steps as high as 0.24 nm, corresponding to an exclusively Ti-rich terminated surface.[43,44] Such structural uniformity is essential for constructing an ideal MoS_2-$SrTiO_3$ heterostructure and largely simplifies the later-on discussions about the interface interactions. After the CVD synthesis, the samples were then subjected to a series of *onsite* characterizations to examine the fabrication results of MoS_2 as well as the surface structures of the $SrTiO_3$ substrate. Figure 1b shows a scanning electron microscopy (SEM) image of the as-prepared MoS_2-$SrTiO_3(111)$ sample which witnesses many triangular-shaped MoS_2 nanosheets that spread for 500 nm to 2 μm and orient either parallelly or antiparallelly to one certain direction, indicative of a typical epitaxial growth of MoS_2 on the $SrTiO_3(111)$ substrate. Further examining the sample surface with AFM reveals a uniform thickness of ~0.87 nm for the as-grown MoS_2 nanosheets, corresponding to the single layer height of MoS_2.[45,46] Simultaneously, the step-terrace structure of the $SrTiO_3(111)$ substrate is clearly viewed, as shown in Figure 1c, manifesting a well-defined atomic structure of the sample surface. To further investigate the atomic details of the MoS_2-$SrTiO_3(111)$ heterostructure, we performed the same synthetic strategy to grow MoS_2 on a Nb-doped $SrTiO_3$ (111) single crystal substrate (shorten as MoS_2-Nb-$SrTiO_3(111)$) and measured with scanning tunneling microscopy (STM). As shown in Figure 1d and SI, Figure S2, atomic resolution can be readily obtained over the triangular MoS_2 nanosheets, which recognizes a hexagonal lattice with 0.32 nm for the periodicity, perfectly consistent with that for MoS_2 as reported in other works.[34,47] One may also notice that although the $SrTiO_3(111)$ surface does not present periodic atomic structure owing to vacancy-induced disordering, the overall surface corrugation is still at the atomic level. Moreover, such substrate corrugation is directly reproduced on the MoS_2 patch (see SI, Figure S2), which in turn reflects that the as-grown MoS_2 nanosheets are strictly intimately attaching to the $SrTiO_3$ (111) surface.[47] This is particularly true for the regions where the MoS_2 carpets over the steps or surface vacancies of the substrate. One can clearly observe a continuous atomic lattice (see Figure S2) once the STM tip is brought close enough to the surface. These microscopic evidence completely testify the clean interfaces of our fabricated samples.

Aside from the microscopic characterizations, elemental and chemical sensitive spectroscopies are necessary for confirming the chemical nature of the synthesized MoS_2 nanosheets. The full-range X-ray photoelectron spectroscopy (XPS) survey spectra of the blank $SrTiO_3(111)$ substrate and the MoS_2-$SrTiO_3(111)$ sample are presented in SI, Figure S3, and Figure 1e, respectively. Comparison of the two spectra clearly shows the pute emergence of Mo and S signals after the CVD

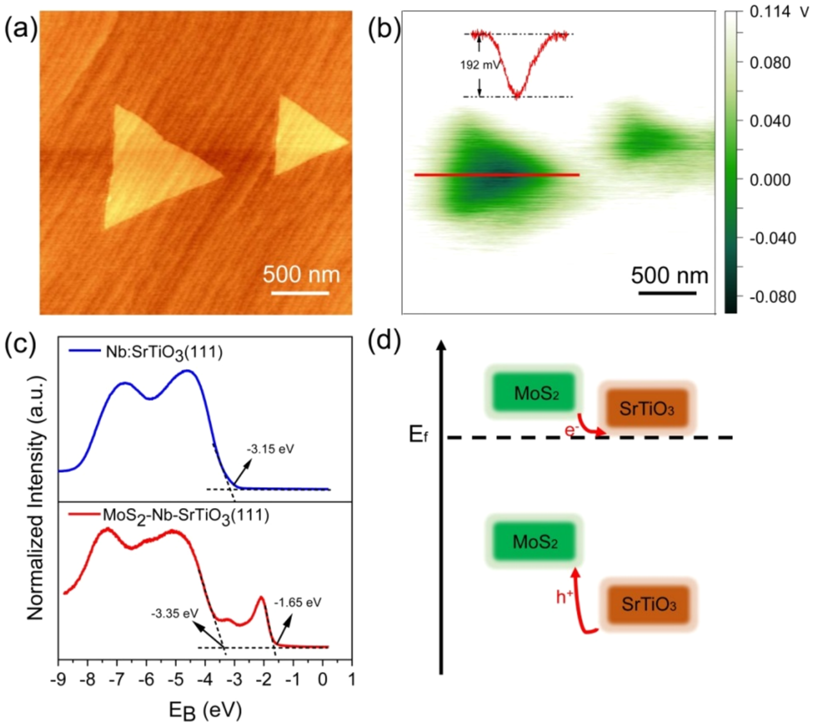

Figure 3. (a) Topography and (b) surface potential images of two selected MoS_2 nanosheets grown on the $SrTiO_3(111)$ substrate. Inset in (b) shows the line profile along the red arrow, confirming the MoS_2 region has a lower surface potential relative to the uncovered $SrTiO_3$ surface. (c) UPS spectra of the Nb:$SrTiO_3(111)$ and Nb-MoS_2-$SrTiO_3$ samples, respectively. (d) Proposed band alignment for the MoS_2/$SrTiO_3(111)$ heterostructure.

synthesis, suggesting the formation of MoS_2 as well as the cleanness of the synthetic process. The only contamination comes from the carbon species, which generally exist for all the sample surfaces experiencing the air exposure. We consider these carbon contaminations are existing at the top surface or defective sites of our fabricated MoS_2-$SrTiO_3(111)$ sample instead of intercalated inside the MoS_2/$SrTiO_3$ interface because the CVD growth of MoS_2 was performed in a carbon free atmosphere and at high temperature. Besides the XPS measurements, we also applied ultraviolet−visible light absorption spectroscopy (UV−vis) on our samples. The results depicted in Figure 1f clearly show that relative to the bare $SrTiO_3(111)$ substrate, the as-prepared MoS_2-$SrTiO_3(111)$ presents significantly enhanced absorption in the visible light region (400−800 nm) with characteristic peaks at around 608 and 656 nm, which corresponds to the specific absorption of MoS_2. Finally, Raman spectroscopy was measured as it is the most compelling spectroscopy for two-dimensional materials. In SI, Figure S4, we show the typical Raman spectrum of our MoS_2-$SrTiO_3(111)$ sample. Unfortunately, because the strong background vibration of the $SrTiO_3(111)$ substrate (in the range of the 380−410 cm^{-1}), the characteristic signals of the MoS_2 nanosheets become unobvious. Alternatively, we follow the same treatment as reported for the MoS_2/TiO_2 heterostructure in our previous study[47] and split and transfer the MoS_2 nanosheets from the MoS_2-$SrTiO_3(111)$ sample to a SiO_2/Si substrate (termed as tr-MoS_2-SiO_2/Si). The inserted picture in SI, Figure S5h, clearly demonstrates that the transfer process is successful and the MoS_2 nanosheets remain triangular shape after transferred onto SiO_2/Si. Figure 1g shows the typical Raman spectrum collected on the tr-MoS_2-SiO_2/Si sample, wherein the characteristic peaks at 384.75 and 403.96 cm^{-1} are clearly identified as the E^1_{2g} and A_{1g} phonon modes of single layer MoS_2, respectively. Moreover, the frequency difference between E^1_{2g} and A_{1g} peaks reads 19.2 cm^{-1}, asserting the AFM conclusion that the synthetic MoS_2 nanosheets are indeed monolayer thick. Actually, we have measured the Raman spectrum at varied positions on the tr-MoS_2-SiO_2/Si sample, all the spectra give similar values for the frequency difference, as shown in SI, Figure S5, indicating a uniformly single layer thickness of MoS_2 throughout the entire surface of the sample. Therefore, the above-mentioned spectroscopy characterizations in all verify that we have constructed high quality MoS_2/$SrTiO_3$ heterostructure with clean and well-defined interface structure.

Charge Transfer and Band Alignment at the MoS_2-$SrTiO_3(111)$ Interface. The intimate contact of MoS_2 with the $SrTiO_3$ surface is essential for unraveling the intrinsic properties of the hybridized system. Our CVD sample has demonstrated a proper platform to investigate the interface interactions of the MoS_2-$SrTiO_3(111)$ heterostructure. One of the chief questions is the charge redistribution at the interface region upon the direct contact of the two materials. To look into this issue, we have carefully analyzed the high resolution XPS spectra of all present elements before and after MoS_2 growth, as shown in Figure 2. It needs to be mentioned that here the binding energy (BE) of the air-exposure-induced carbon species is fixed to 284.8 eV, which provides a reference for discussion of all other elements. First, both Mo and S appears only for the MoS_2-$SrTiO_3$ (111) sample, while the blank $SrTiO_3(111)$ crystal presents no detectable signals. The Mo 3*d* spectrum in Figure 2a shows two prominent peaks with binding energies of 230.0 and 233.25 eV, consistent with the literature reports for the $3d_{5/2}$ and $3d_{3/2}$ components of Mo^{4+}, respectively.[29] The weak peaking signals at around 227.0 eV can be attributed to S 1*s* transitions. In Figure 2b, the two peaks at 162.9 and 164.1 eV of the MoS_2-$SrTiO_3(111)$ can be assigned to S $2p_{3/2}$ and S $2p_{1/2}$ for S^{2-} chemical state, respectively, also agreeing well with values reported for MoS_2 in the previous studies.[29] Concerning the XPS of other elements including Sr, Ti, and O, as shown in Figure 2c−e, they appear for both the MoS_2-$SrTiO_3(111)$ and the blank $SrTiO_3$ samples. One can clearly see a prominent blue-shift occurring for all three elements of the MoS_2-$SrTiO_3(111)$ sample as compared to the bare $SrTiO_3$ substrate. In SI, Figure S6, we present detailed comparison of the XPS profiles of Sr 3*d*, Ti 2*p*, and O 1*s* in the two samples, respectively. One can find the line shapes of all three elements are basically maintained throughout the MoS_2 synthesis, consistent with the preserved atomic flatness of the TiO_x terminated $SrTiO_3(111)$ surface. However, a slight yet visible discrepancy can be recognized for the Sr 3*d* spectra. As displayed by the peak fittings in SI, Figure S7a,b, the spectrum of blank $SrTiO_3(111)$ shows only one set of XPS peaks centering at 134.76 and 133.00 eV, while that of MoS_2-$SrTiO_3(111)$ can be best fitted with two sets of peaks, the main set of which has blue-shifted by ~0.8 eV to 135.56 and 133.80 eV, while the emerged minor set appears at 136.70 and 134.53 eV, respectively. These minor Sr species may probably correspond to the surface SrO_x species that has been formed upon segregation of Sr ions from the bulk of $SrTiO_3$ to the surface during the CVD procedure at high temperature.[48,49] As corroborated by the AFM image in SI, Figure S7c, these SrO_x species clearly avoid the MoS_2 region and reside only on the uncovered $SrTiO_3$ surface. Their existence should not affect the interface interactions between the MoS_2 and $SrTiO_3$ at the interface. In Figure 2f, we plot the measured differences in the binding energies for the two different samples, which interestingly depicts an equivalent value of 0.7−0.8 eV for all three elements. We propose that such unified binding energy shifts are attributed to the static electrical field which is established at the interface between the two materials upon their contact with each other. Similar effects have also been visualized in our previous studies of graphene/TiO_2 and MoS_2/TiO_2 heterostructures, wherein the interfaces are dominated by the physical interactions instead of any chemical bonding.[47,50]

The XPS-suggested interface dipole field should come from the charge redistribution between MoS_2 and $SrTiO_3$ because the two materials possess different work function (WF). To elucidate the actual situation of the MoS_2/$SrTiO_3$ heterojunction, we have performed Kelvin-probe force microscopy (KPFM) measurements on the as-prepared sample. Figure 3 shows the KPFM image of a selected region on the MoS_2-$SrTiO_3(111)$ sample, which clearly reveals that the MoS_2 nanosheets have lower surface potential (SP) than the $SrTiO_3$ substrate. In addition, the larger MoS_2, the lower SP at the center of the MoS_2 nanosheet. This result manifests that the MoS_2 has relatively lower WF and thus may transfer electrons into the $SrTiO_3$ substrate at the contact region. In this picture, the charge transfer occurring at the interface of the MoS_2/$SrTiO_3$ should formulate a downward dipole field along the surface normal, which subsequently causes a downward band-bending at the heterojunction interface. As a consequence, the core levels of the substrate elements all experience a downward shift relative to the aligned Fermi level and thus exhibit blue-shifts relative to the bare $SrTiO_3$ surface without MoS_2. It needs to be mentioned that charge redistribution generally exists for any heterojunction of two materials with different WFs, which usually plays important roles in tuning the electronic properties of the hybridized system. Particularly for the compositional systems of TMDs and oxides, such phenomenon can provide an efficient strategy to control the charge carriers, the photovoltaic, the photoluminescence as well as the catalytic activities of the TMDs materials via tuning the electronic interactions from the oxide substrates.[32,51,52]

On the basis of the charge transfer and band-bending picture as derived by KPFM and XPS, we would further determine band levels of both MoS_2 and $SrTiO_3$ relative to the aligned Fermi level, which usually plays a critical role in determining the potential applications of the hybridized semiconductors. To do this, we have applied ultraviolet photoelectron spectroscopy (UPS) measurements on both Nb:$SrTiO_3(111)$ and MoS_2-Nb-$SrTiO_3(111)$ samples to examine their valence bands. From the blue curve in Figure 3c, we can identify the valence band maximum (VBM) of the Nb:$SrTiO_3(111)$ at −3.15 eV below Fermi level. For the hybridized sample of MoS_2-Nb-$SrTiO_3(111)$ (the red curve), the VBM is recognized at −1.65 eV, which can be ascribed to the sole contribution from MoS_2 (mainly Mo 3*d*). In the meantime, the band edge of the $SrTiO_3$ has downshifted to ~ −3.35 eV with MoS_2 in presence. Despite of the immeasurable conduction band edges of the samples, we may already picture the band alignments of the MoS_2/$SrTiO_3$ heterostructure after involving the band gaps of the two materials. If we propose the intrinsic band structures of both MoS_2 and $SrTiO_3$ are not changed very much in the heterostructure considering the physical nature of the interface interaction, we can take the band gap values of isolated material for estimation. It is well-known the band gap of single-layer MoS_2 is 1.85 eV and that of bulk $SrTiO_3$ is 3.4 eV, respectively.[3,53,54] Therefore, the conduction band minimum (CBM) of MoS_2 and $SrTiO_3$ can be determined at 0.2 and ~0.05 eV above the Fermi level of the MoS_2-$SrTiO_3$ heterostructure. The band alignment can thus be schemed as a type-II heterojunction as shown in Figure 3d. The higher CBM level of the MoS_2 relative to $SrTiO_3$ indicates that MoS_2 may donate electrons into the latter, hence possessing a relatively lower surface potential, which is consistet with the KPFM measurement as shown in Figure 3b. Another notable feature in Figure 3d is that the CBMs of MoS_2 and $SrTiO_3$ are both positioned close to the Fermi level, indicating a strongly *n*-type doped nature for both materials in the hybridized system. This picture also gets supported by our measurements of scanning tunneling spectroscopy as shown in SI, Figure S8. Therefore, the self-consistency of our systematic characterizations has clearly demonstrated that the as-grown MoS_2 is *n*-type doped and serves as an electron donor in the CVD-fabricated MoS_2-$SrTiO_3$ heterostructure.

Optical Properties of the MoS_2-$SrTiO_3$ Heterostructure. The optical property is one of the most attractive properties of the TMD materials including MoS_2. Particularly, their hybridization with other materials can provide a versatile manipulation strategy to tailor the intrinsic optical properties of TMDs. Therefore, the MoS_2/$SrTiO_3$ sample was carefully measured with photoluminescence (PL) spectroscopy to examine the tuning effect of the $SrTiO_3$ substrate. First, PL spectra were collected at different positions of the as-prepared MoS_2-$SrTiO_3(111)$ sample at room temperature, as shown in SI, Figure S9, which constantly gives a single luminescing peak at around 658 nm despite the varied intensities. This PL peak can be assigned to the main optical transition resulted from the

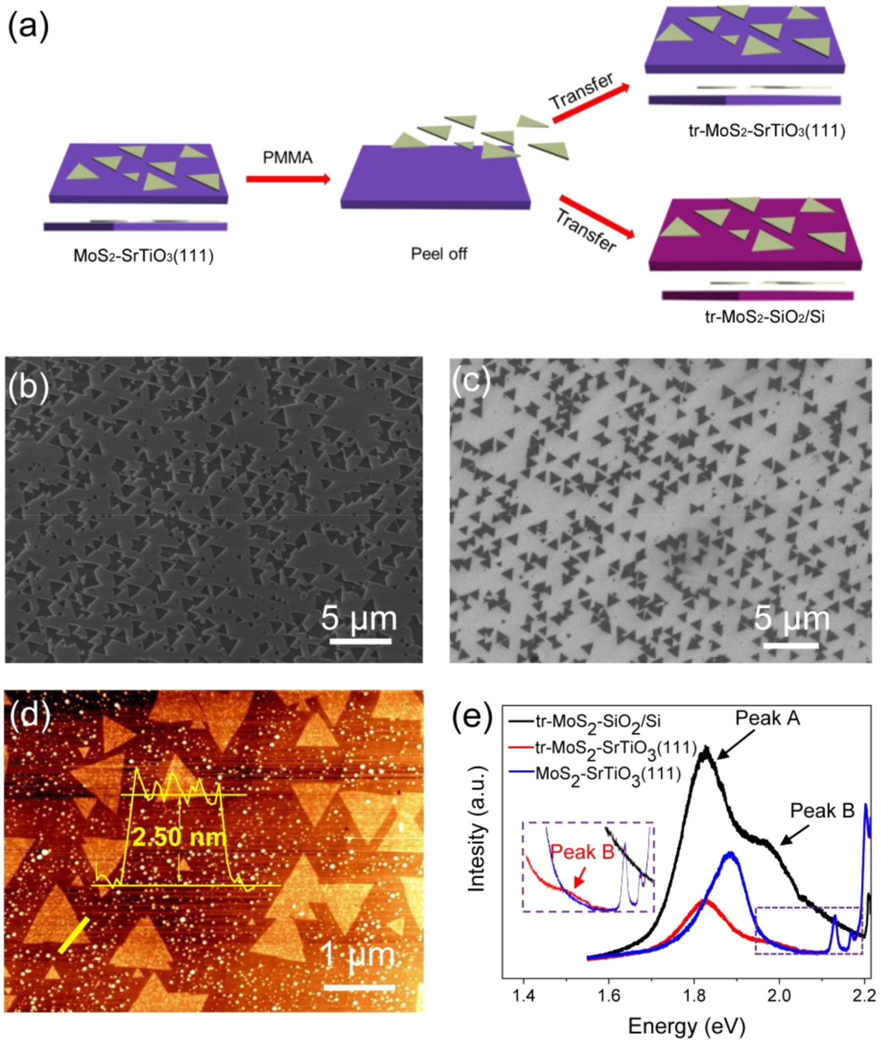

Figure 4. (a) Schematic illustration for transfer process. (b) SEM image of the MoS_2 nanosheets after transfer to a SiO_2/Si substrate. (c) SEM and (d) AFM images of MoS_2 nanosheets after transfer to a $SrTiO_3(111)$ substrate. Inset in (d) shows the height profile along the yellow line across a piece of MoS_2 nanosheet, indicating the transfer process leads to the ruin of the interface. (e) Room temperature PL spectra of MoS_2-$SrTiO_3(111)$, tr-MoS_2-SiO_2/Si, and tr-MoS_2-$SrTiO_3(111)$ samples, respectively. Inset is the magnified spectrum region showing the appearance of B peak in the tr-MoS_2-$SrTiO_3(111)$ sample.

excitation from the band edges, which confirms that the MoS_2 nanosheets have a single-layer thickness and a uniform distribution over the entire $SrTiO_3$ surface. Moreover, SI, Figure S10, shows the PL mapping of an individual MoS_2 triangle, which was taken at the peaking wavelength of 1.88 eV. The uniform contrast across the whole MoS_2 triangle once again certifies the high crystallinity of the MoS_2 nanosheet. Another noticeable characteristic of the PL spectra is the absence of signals for B excitons, which is similar to what we found for the MoS_2/TiO_2 hybridized system.[47] At the present stage, we propose the B excitons should decay through other channels instead of luminescing in these CVD-prepared heterostructures.

For better elucidating the effect of the $SrTiO_3$ on the optical property of MoS_2, we peel the MoS_2 nanosheets off and transferred them onto a blank $SrTiO_3$ (111) (termed as tr-MoS_2-$SrTiO_3(111)$) and SiO_2/Si (termed as tr-MoS_2-SiO_2/Si) substrate, respectively, and measured their PL for comparison. Figure 4a shows the schematic of the transfer process, which is detailedly described in the Experimental Section. Parts b and c of Figure 4 show the SEM images of tr-MoS_2-SiO_2/Si and tr-MoS_2-$SrTiO_3(111)$ samples, respectively, both evidencing the well-preserved triangular-shaped MoS_2 nanosheets, thus manifesting a successful transfer operation. The AFM image in Figure 4d clearly observes the triangular MoS_2 nanosheets that have been transferred onto the bare $SrTiO_3(111)$ surface. However, the original step-terrace structure as well as the overall atomic flatness of the $SrTiO_3(111)$ substrate is lost; scattered bright protrusive species concomitantly appeared which can be attributed to the adsorbed impurities during the transfer operation. Moreover, the height profile across the MoS_2 nanosheet is now measured as 2.5 nm, strongly suggesting a layer of molecules (as thick as 1.5 nm) has been intercalated between MoS_2 and the $SrTiO_3$ substrate. Afterward, the PL spectrum of the tr-MoS_2-$SrTiO_3(111)$ sample now shows drastic difference against that of the as-prepared MoS_2-$SrTiO_3(111)$ sample but basically reproduces the same profile as that of the tr-MoS_2-SiO_2/Si sample. Moreover, the PL of tr-MoS_2-$SrTiO_3(111)$ displays an obviously reduced intensity while the main peak red-shifts to 1.83 eV. In addition, the B exciton now appears at around 1.97 eV after transfer. All these facts direct to the intercalated

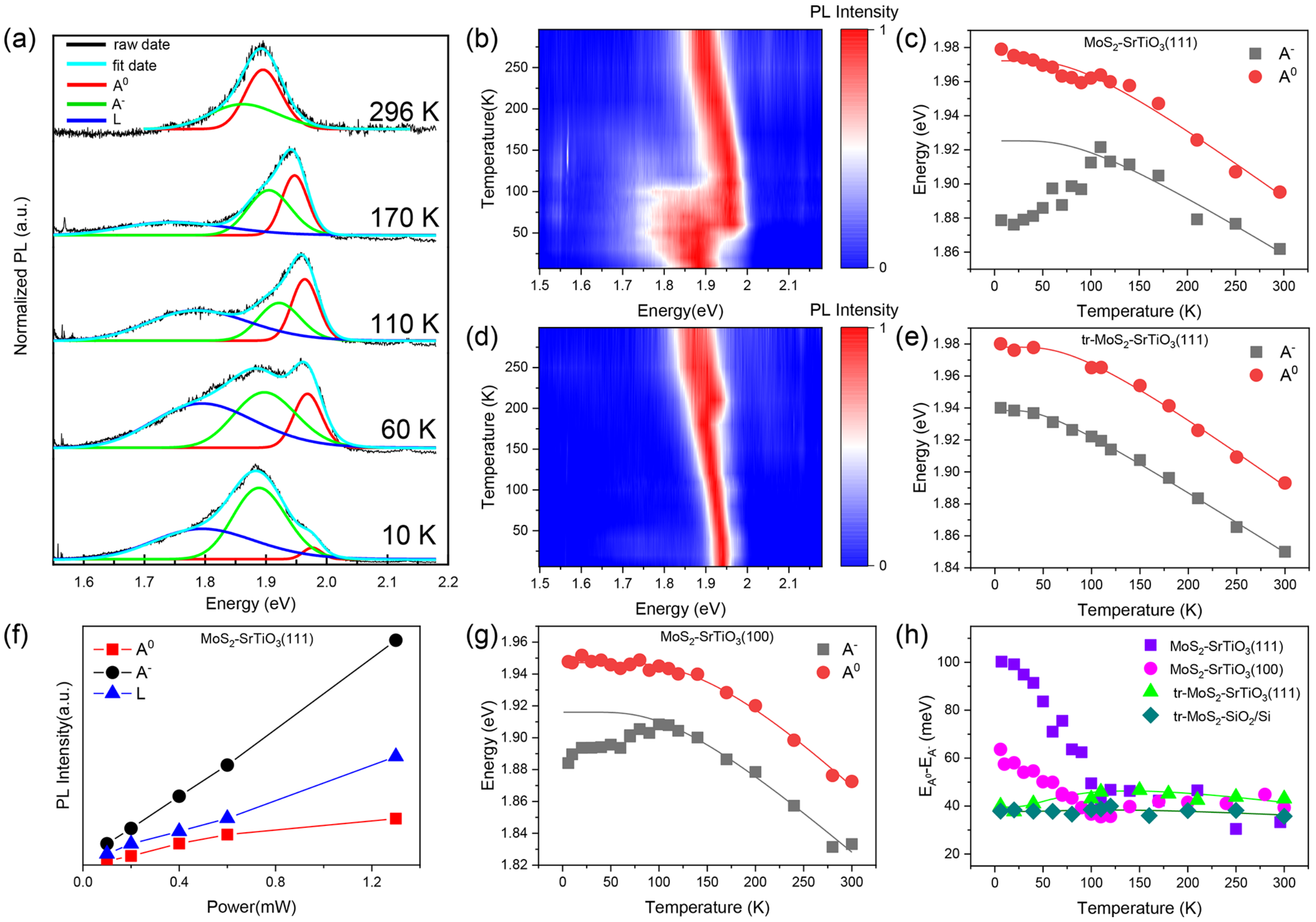

Figure 5. (a) PL emission of the MoS_2-$SrTiO_3(111)$ taken at 296, 170, 110, 60, and 10 K, respectively. Each spectrum is fitted with compositional emissions originated from exciton A^0 (red), trion A^- (green), and the local defect L (blue). (b) Pseudocolor map of variable temperature PL spectra of the MoS_2-$SrTiO_3(111)$ sample ranging from 296 to 10 K. (c) Plot of the peak energies of both A^0 and A^- quasiparticles in the MoS_2-$SrTiO_3(111)$ sample as a function of temperature, (d) Pseudocolor map of variable temperature (296−10 K) PL emission taken on the tr-MoS_2-$SrTiO_3(111)$ sample. (e) Plot of the peak energies of both A^0 and A^- quasiparticles in tr-MoS_2-$SrTiO_3(111)$ as a function of temperature. (f) Power-dependent evolution of the A^0, A^-, and L peaks for the MoS_2-$SrTiO_3(111)$ sample at 10 K. (g) Plot of the peak energies of both A^0 and A^- quasiparticles in a MoS_2-$SrTiO_3(100)$ sample as a function of temperature. (h) Temperature dependence of the binding energies of A^- exciton ($E_{A^0} - E_{A^-}$) in various samples including MoS_2-$SrTiO_3(111)$, MoS_2-$SrTiO_3(100)$, tr-MoS_2-$SrTiO_3(111)$, and tr-MoS_2-SiO_2/Si.

species, which were introduced during the transfer process. We propose that these species have somehow isolated the interactions of the $SrTiO_3$ substrate to the MoS_2 adlayer, and bring them to the similar case as the MoS_2-SiO_2/Si interface. These results have clearly demonstrated that the cleanness of the interface can definitely influence the physicochemical property of a hybridized system. On the other hand, it also unambiguously verifies the significant tuning effect of the $SrTiO_3$ substrate over the MoS_2 adlayer.

Insights of MoS_2/$SrTiO_3$ Interface Interactions by Temperature-Dependent PL. To further understand the physical mechanism behind the modulation effect of the $SrTiO_3(111)$ substrate over the monolayer MoS_2, we resorted to detailed variable-temperature PL measurements of the hybrid systems. Figure 5a shows a series of representative PL spectra taken on the MoS_2-$SrTiO_3(111)$ sample at 296, 170, 110, 60, and 10 K, respectively. The rest of the results of other temperatures can be found in SI, Figure S11. Note here all the spectra have been deconvoluted by following a multipeak fitting. The red, green, and blue counterparts are designated as A^0, A^-, and L excitons, respectively, while the B exciton is absent throughout the measurements. A^- exciton is the combination of A^0 with one electron, while the L exciton is correlated with the specific photoluminescence owing to the existing defects or strains within the MoS_2 film.[33,34] As shown in Figure 5a, the spectrum of 296 K is dominated by A^0 peak positioning at 1.895 eV. Concomitantly, the A^- peak is half weak and positioned at 1.862 eV. Along with the decreasing of the temperature, the A^0 peak gradually shrinks and shifts to higher energy, while the A^- peak gets stronger and stronger until finally dominates the PL spectrum at close to 10 K. Accompanying these changes is the appearance and stepwise growing of the broad L peak at around 1.75−1.80 eV, which becomes more and more prominent at low temperatures. All these temperature-related PL evolution can be more clearly visualized with the pseudocolor map that is shown in Figure 5b, wherein an abrupt inflection is visualized at around 100−50 K, which reflects a drastic red-shift of the main PL occurring at this particular temperature range. Figure 5c plots the energies of both A^0 and A^- excitons versus the temperature. Clearly, the A^0 exciton blue-shifts from 1.895 to 1.979 eV all the way down with the temperature changing from 295 to 10 K, whereas the

https://doi.org/10.1021/acsnano.1c00482
ACS Nano 2021, 15, 8610−8620

A^- exciton follows this trend at the beginning yet turns the direction (red-shifts) sharply at around 110 K. Finally, at 10 K, the binding energy (BE) of the A^- exciton (defined as the energy difference relative to that of A exciton) accumulates to around 100 meV, which is extraordinarily larger than the usual BE of the negatively charged excitons in TMDs. Besides, to confirm the facticity of these excitons, we measured the PL spectroscopy with variable power at 10 K. As can be seen in Figure 5f, the peak intensities of A^0, A^-, and L excitons increase simultaneously with the increment of the power (from 0.1 mW to 1.3 mW) and scale almost linearly without crossing each other. This fact indicates that the observed temperature-dependent PL changes should be independent of the incident laser powers. Actually, S. Sarkar and co-workers have recently observed similar phenomena on the CVD-grown MoS_2 films on different $SrTiO_3$ single crystal substrates.[27,28] They attributed the remarkable enhancement in the BE of A^- exciton in MoS_2 to the Fröhlich coupling with the rotational phonons of the tetragonal $SrTiO_3$ crystal, which transformed from the cubic phase under a critical temperature of 135 K. They also found that the (111) facet of $SrTiO_3$ can exert the strongest effect which leads to an overall BE increment of 90 meV at 10 K. This value is significantly lower than what we have obtained (100 meV). Moreover, our measured turning point (110 K) is much closer to the theoretical phase transition temperature of the $SrTiO_3$ crystal (105 K). We notice that in the works of S. Sarkar et al., the authors claimed the high quality of the as-grown MoS_2 film yet showed no evidence of surface cleanness of the $SrTiO_3$ substrates.[27,28] This is the major difference against our samples wherein both the MoS_2 adlayer and the $SrTiO_3$ substrate have been confirmed with ultimate cleanness and flatness. Therefore, we can understand that the ideality of the $MoS_2/SrTiO_3$ interface is critical for the optimized properties of the hybridized system. As a matter of fact, in a control experiment, we transferred the CVD-grown MoS_2 film onto an as-prepared $SrTiO_3(111)$ substrate through a wet method and then subjected to the variable temperature PL measurements (see SI, Figure S12, for the full spectra). Interestingly, the "Z" shape has completely disappeared from the pseudocolor map in Figure 5d. In addition, the plot in Figure 5e clearly shows the energy of A^- blue-shift all the way as A^0 does along with the decreasing of the temperature, both basically falls into the same pattern as the reference samples of the CVD-grown MoS_2-SiO_2/Si and tr-MoS_2-SiO_2/Si (see SI, Figures S13, S14, and S15, for the corresponding results). One may notice that the surface of the as-prepared tr-MoS_2-$SrTiO_3(111)$ sample is not clean (see Figure 4d) due to the deposited contaminations during the transferring procedure. However, these surface contaminations can actually be removed by annealing treatments. As shown by the AFM image in SI, Figure S16, the annealed tr-MoS_2-$SrTiO_3(111)$ sample reproduced the atomic flatness on both the MoS_2 nanosheets and the $SrTiO_3(111)$ terrace. However, the measured height of the MoS_2 still read around 1.0 nm, indicating some intercalated molecules remained at the interface region. Consequently, the variable temperature PL spectra (SI, Figure S16) showed more or less the same as those for the untreated sample, wherein no obvious substrate effects were observed. These results not only confirm the necessity of $SrTiO_3$ substrate for the prominent tuning effect but also emphasize that the cleanness of the interface is critical for validating the so-called Fröhlich coupling between MoS_2 and $SrTiO_3$.

To make our results more persuasive, we also synthesize MoS_2 film on the $SrTiO_3(100)$ single crystal by following the same CVD strategy. As shown in SI, Figure S17, the fabricated MoS_2-$SrTiO_3(100)$ possesses a similarly high quality of the interface which is represented by the triangular shape of the single-layer MoS_2 nanosheets and the atomic flatness of the $SrTiO_3(100)$ substrate (see the detailed characterization results in SI, Figure S17). However, the as-grown MoS_2 sheets adopt an overall disordered orientations, indicating a weaker epitaxial relationships with the $SrTiO_3(100)$ substrate. On this MoS_2-$SrTiO_3(100)$ sample, we also measured the variable-temperature PL as shown in SI, Figure S18, and further concluded as a pseudocolor map in SI, Figure S19. In Figure 5g, we plot the energies of the deconvoluted A^0 and A^- excitons against the temperature, which present similar trends as that derived from the MoS_2-$SrTiO_3(111)$ sample. In other words, one can also see the energy of the A^0 exciton increases monotonically with the temperature decreasing, while the A^- exciton first follows the trend and then reverses the direction below ∼110 K. The biggest difference lies in the changed values of these excitons. Compared to those of the MoS_2-$SrTiO_3(111)$ sample, the A^0 exciton of MoS_2-$SrTiO_3(100)$ has relatively lower while the A^- exciton relatively higher energy. This leads to a reduced BE of A^- exciton of 65 meV (compared with 100 meV for the MoS_2-$SrTiO_3(111)$ sample) at 10 K, which can be explained by the reduced Fröhlich coupling between the MoS_2 and the $SrTiO_3$ substrate. However, we also notice that our result is significantly higher than what Sarkar *et al.* has achieved in their recent study.[27,28] Again, this improvement can be ascribed to our high quality interface with both atomic flatness and high cleanness.

In Figure 5h, we summarize the BE of the A^- exciton ($E_{A^0} - E_{A^-}$) in the aforementioned four different samples. As can be seen, along with the decreasing temperature both MoS_2-$SrTiO_3(111)$ and MoS_2-$SrTiO_3(100)$ show monotonically increased BE once the temperature is lower than 110 K, and the former shows the biggest value of 100 meV for the as-prepared monolayer MoS_2 nanosheets, which can be attributed to the strongest coupling interaction from the polar substrate. For the referenced samples of tr-MoS_2-$SrTiO_3(111)$, its ($E_{A^0} - E_{A^-}$) data basically reproduce another reference sample of tr-MoS_2-SiO_2/Si, wherein no such tuning effect can be observed. This result clearly demonstrates that the interface effect can be completely discriminated by the intercalated species at the interface.

CONCLUSION

In summary, by optimizing CVD synthetic parameters, we have successfully fabricated high quality single layer MoS_2 nanosheets on the atomically flat $SrTiO_3$ (111) substrate, thus constituting a well-defined $MoS_2/SrTiO_3$ heterostructure with clear atomic structure of the interface. Our systematic characterizations demonstrate that in the hybridized system no chemical bonds are formed between MoS_2 and $SrTiO_3$, whereas the obvious charge transfer from MoS_2 to $SrTiO_3$ is present and leads to formation of strong interface dipole field. In addition, the ideal interface structure is found to largely facilitate the electronic−phonon coupling between MoS_2 and $SrTiO_3$, which leads to a significant enhancement of the binding energy and the photoluminescence of the negatively charged exciton. In contrast, such effect can be completely diminished *via* introducing intercalated contaminations which are inevitable for the *ex situ* samples prepared by transfer processes in solution. Therefore, in this work we not only develop a strategy for fabricating ideal heterostructures of TMDs and functional transition metal oxides but also demonstrate that quality control of the interface at atomic level can be critical for realizing the tuning effects of the functional substrates. Moreover, the unexpected coupling effects of $SrTiO_3$ over MoS_2 may bring us a fresh method in tuning the electronic/optical properties of the TMDs for potential applications.

EXPERIMENTAL SECTION

Materials. The $SrTiO_3(111)$ and $SrTiO_3(100)$ single crystals and silica substrate (SiO_2/Si) were purchased from Hefei KeJing Material Technology Co., Ltd. Sulfur powder (99.6%) and MoO_3 powder (99.6%) were purchased from Aladdin Co., Ltd. Hydrofluoric acid (40%), acetone (99.5%), and ammonium fluoride (>96%) were purchased from Sinopharm Chemical Reagent Co., Ltd. All of the chemicals above were used as received without further treatment.

Preparation of Atomically Flat $SrTiO_3$ Surfaces. Atomically smooth surfaces of $SrTiO_3(111)$ and $SrTiO_3(100)$ were routinely prepared by referring to the reported recipe,[43,44] which went through ultrasonic with ultrapure water for 10 min, etching with buffered hydrogen fluoride (BHF) solution for 20 min, rinsing with deionized water (Millipore, 18 MΩ•cm), drying in a nitrogen (high purity, 99.999%) stream, and annealing at 1000 °C for 1.5 h in air. The atomic flatness and cleanness of the prepared surfaces were confirmed by AFM and XPS measurements repeatedly.

Growth of Monolayer MoS_2 Nanosheets on the $SrTiO_3$ Single Crystal Surface. A tube furnace (OTF-1200X, Hefei Kejing Material Technology Co., Ltd.) with two heating zones was used for the CVD growth of MoS_2 on $SrTiO_3$. The precursors of S and MoO_3 powders were placed in quartz boats at the upstream and downstream zones, respectively. The MoO_3 carrier was designed with a special holder to support the facing-down $SrTiO_3$ crystal. Before any growth the reaction system was flushed with high purity N_2 (~300 sccm for the flow rate). Then the S powder was gradually heated to 200 °C to vaporize and the S vapor was carried by N_2 (reduced to ~10 sccm) to the next reaction zone. Meanwhile, the MoO_3 powder was heated to 700 °C to vaporize and react with the incoming S vapor for certain time. After turning off the heating power, the furnace was kept closed until the temperature reaches ~570 °C. Then the cover was opened and the whole system was allowed to cool down naturally to room temperature under the N_2 flux (turn back to 300 sccm again).

Transfer Method for Monolayer MoS_2 Nanosheets on SiO_2/Si and $SrTiO_3$ (111) Substrates. The as-grown MoS_2 nanosheets can be transferred onto discretionary substrates through a general wet method as described in our previous paper. First the top of the MoS_2-$SrTiO_3(111)$ sample was spin-coated with a thin layer of poly(methyl methacrylate) (PMMA). Then the PMMA covered sample was dipped into a HF solution (~20%) for etching for certain time. After that, the sample was further transferred into deionized water and immersed for 10−15 min. Normally, the PMMA film attached with the MoS_2 nanosheets can detach automatically from the $SrTiO_3$ substrate and float on the water surface. Next, SiO_2/Si and $SrTiO_3$ or whatever other substrates can be grabbed by a pincette were carefully held up to this film. To remove the PMMA film for the last step, one needed to place the transferred sample in acetone for 24 h.

Characterizations. The AFM measurements were performed on a Multimode V (Bruker Co.) with commercial silicon cantilevers (Bruker Co.). Particularly, the KPFM was measured with As-doped silicon tips with different coatings (SCM-PIT-V2, Bruker Co.). STM was measured with a commercial low-temperature STM (Createc Co.) at liquid nitrogen temperature. UV−vis absorption spectra were acquired on a SolidSpec-3700 spectrometer (Shimazu). SEM measurements were performed using a SU8220 model instrument. The XPS was measured with an ESCALAB 250Xi (Thermo Fisher Scientific) equipped with an Al Kα source (1486.7 eV). Variable temperature PL spectra were collected using an IsoPlane SCT 320 spectrometer (Princeton) incorporated on a home-built vacuum system. The sample temperature was controlled by a commercial workstation connected to a cryostat (Montana Instruments). The incident laser had a wavelength of 532 nm and a tunable power below 100 μW. For the PL mapping measurements, a 100× objective lens was applied to focus the laser point to as small as 3 μm for the diameter and scanned over a selected area on the sample. Raman spectroscopy was measured using a LabRam HR Evolution with incident laser of 532 nm for the wavelength as well. UPS spectra were collected at BL13U endstation of National Synchrotron Radiation Laboratory (NSRL).

ASSOCIATED CONTENT

Supporting Information

The Supporting Information is available free of charge at https://pubs.acs.org/doi/10.1021/acsnano.1c00482.

Additional characterization results including AFM, STM, SEM, and PL measurements for different samples are provided (PDF)

AUTHOR INFORMATION

Corresponding Authors

Xiang Shao − *Department of Chemical Physics, Synergetic Innovation Center of Quantum Information and Quantum Physics, and CAS Key Laboratory of Urban Pollutant Conversion, University of Science and Technology of China, Hefei, Anhui 230026, China;* orcid.org/0000-0002-8768-4366; Email: shaox@ustc.edu.cn

Hualing Zeng − *International Center for Quantum Design of Functional Materials (ICQD), Hefei National Laboratory for Physical Sciences at the Microscale, Key Laboratory of Strongly-Coupled Quantum Matter Physics, Chinese Academy of Sciences, Department of Physics, and Synergetic Innovation Center of Quantum Information and Quantum Physics, University of Science and Technology of China, Hefei, Anhui 230026, China;* orcid.org/0000-0001-5869-9553; Email: hlzeng@ustc.edu.cn

Authors

Chenxi Huang − *Department of Chemical Physics, University of Science and Technology of China, Hefei, Anhui 230026, China*

Jun Fu − *International Center for Quantum Design of Functional Materials (ICQD), Hefei National Laboratory for Physical Sciences at the Microscale, Key Laboratory of Strongly-Coupled Quantum Matter Physics, Chinese Academy of Sciences, Department of Physics, and Synergetic Innovation Center of Quantum Information and Quantum Physics, University of Science and Technology of China, Hefei, Anhui 230026, China*

Miaomiao Xiang − *Department of Chemical Physics, University of Science and Technology of China, Hefei, Anhui 230026, China*

Jiefu Zhang − *Department of Chemical Physics, University of Science and Technology of China, Hefei, Anhui 230026, China*

Complete contact information is available at: https://pubs.acs.org/10.1021/acsnano.1c00482

Author Contributions

C.H. and J.F. contributed equally to this work

Notes

The authors declare no competing financial interest.

ACKNOWLEDGMENTS

We are grateful to the financial support of the National Key Research and Development Program of China (grant no. 2017YFA0205003, 2017YFA0205004), NSFC (grant no. 21872130, 91545128), the Fundamental Research Funds for the Central Universities of China (grant no. WK3510000013 and WK2060190084), and Anhui Initiative in Quantum Information Technologies (grant no. AHY170000). We also thank the support from the NSRL at Hefei.

REFERENCES

(1) Kang, K. T.; Park, J.; Suh, D.; Choi, W. S. Synergetic Behavior in 2D Layered Material/Complex Oxide Heterostructures. *Adv. Mater.* **2019**, *31*, 1803732.

(2) Huang, M. H.; Madasu, M. Facet-Dependent and Interfacial Plane-Related Photocatalytic Behaviors of Semiconductor Nanocrystals and Heterostructures. *Nano Today* **2019**, *28*, 100768.

(3) Huang, Z.; Ariando; Renshaw Wang, X.; Rusydi, A.; Chen, J.; Yang, H.; Venkatesan, T. Interface Engineering and Emergent Phenomena in Oxide Heterostructures. *Adv. Mater.* **2018**, *30*, 1802439.

(4) Tahir, M.; Tasleem, S.; Tahir, B. Recent Development in Band Engineering of Binary Semiconductor Materials for Solar Driven Photocatalytic Hydrogen Production. *Int. J. Hydrogen Energy* **2020**, *45*, 15985−16038.

(5) Zhang, Z.; Bai, L.; Li, Z.; Qu, Y.; Jing, L. Review of Strategies for the Fabrication of Heterojunctional Nanocomposites as Efficient Visible-Light Catalysts by Modulating Excited Electrons with Appropriate Thermodynamic Energy. *J. Mater. Chem. A* **2019**, *7*, 10879−10897.

(6) Tang, P.; Arbiol, J. Engineering Surface States of Hematite Based Photoanodes for Boosting Photoelectrochemical Water Splitting. *Nanoscale Horiz.* **2019**, *4*, 1256−1276.

(7) Su, Q.; Li, Y.; Hu, R.; Song, F.; Liu, S.; Guo, C.; Zhu, S.; Liu, W.; Pan, J. Heterojunction Photocatalysts Based on 2D Materials: The Role of Configuration. *Adv. Sustainable Syst.* **2020**, *4*, 2000130.

(8) Xie, C.; Liu, C. K.; Loi, H. L.; Yan, F. Perovskite-Based Phototransistors and Hybrid Photodetectors. *Adv. Funct. Mater.* **2020**, *30*, 1903907.

(9) Chen, H.; Millis, A. Charge Transfer Driven Emergent Phenomena in Oxide Heterostructures. *J. Phys.: Condens. Matter* **2017**, *29*, 243001.

(10) Yang, Z.; Hao, J. Recent Progress in 2D Layered III−VI Semiconductors and Their Heterostructures for Optoelectronic Device Applications. *Adv. Mater. Technol.* **2019**, *4*, 1900108.

(11) Jeong, M. H.; Sun, J.; Young Han, G.; Lee, D. H.; Bae, J. W. Successive Reduction-Oxidation Activity of FeOx/TiO_2 for Dehydrogenation of Ethane and Subsequent CO_2 Activation. *Appl. Catal., B* **2020**, *270*, 118887.

(12) Chica, B.; Wu, C.-H.; Liu, Y.; Adams, M. W. W.; Lian, T.; Dyer, R. B. Balancing Electron Transfer Rate and Driving Force for Efficient Photocatalytic Hydrogen Production in CdSe/CdS Nanorod−[NiFe] Hydrogenase Assemblies. *Energy Environ. Sci.* **2017**, *10*, 2245−2255.

(13) Hu, L.; Yan, J.; Liao, M.; Xiang, H.; Gong, X.; Zhang, L.; Fang, X. An Optimized Ultraviolet-A Light Photodetector with Wide-Range Photoresponse Based on ZnS/ZnO Biaxial Nanobelt. *Adv. Mater.* **2012**, *24*, 2305−2309.

(14) Duan, X.; Wang, C.; Shaw, J. C.; Cheng, R.; Chen, Y.; Li, H.; Wu, X.; Tang, Y.; Zhang, Q.; Pan, A.; Jiang, J.; Yu, R.; Huang, Y.; Duan, X. Lateral Epitaxial Growth of Two-Dimensional Layered Semiconductor Heterojunctions. *Nat. Nanotechnol.* **2014**, *9*, 1024−1030.

(15) Singh, G.; Jouan, A.; Herranz, G.; Scigaj, M.; Sanchez, F.; Benfatto, L.; Caprara, S.; Grilli, M.; Saiz, G.; Couedo, F.; Feuillet-Palma, C.; Lesueur, J.; Bergeal, N. Gap Suppression at a Lifshitz Transition in a Multi-Condensate Superconductor. *Nat. Mater.* **2019**, *18*, 948−954.

(16) Xu, C.; Ravi Anusuyadevi, P.; Aymonier, C.; Luque, R.; Marre, S. Nanostructured Materials for Photocatalysis. *Chem. Soc. Rev.* **2019**, *48*, 3868−3902.

(17) Liao, J. F.; Wu, W. Q.; Jiang, Y.; Zhong, J. X.; Wang, L.; Kuang, D. B. Understanding of Carrier Dynamics, Heterojunction Merits and Device Physics: Towards Designing Efficient Carrier Transport Layer-Free Perovskite Solar Cells. *Chem. Soc. Rev.* **2020**, *49*, 354−381.

(18) Trier, F.; Christensen, D. V.; Pryds, N. Electron Mobility in Oxide Heterostructures. *J. Phys. D: Appl. Phys.* **2018**, *51*, 293002.

(19) Lin, L.; Deng, B.; Sun, J.; Peng, H.; Liu, Z. Bridging the Gap between Reality and Ideal in Chemical Vapor Deposition Growth of Graphene. *Chem. Rev.* **2018**, *118*, 9281−9343.

(20) Sakthivel, T.; Huang, X.; Wu, Y.; Rtimi, S. Recent Progress in Black Phosphorus Nanostructures as Environmental Photocatalysts. *Chem. Eng. J.* **2020**, *379*, 122297.

(21) Hu, Z.; Wu, Z.; Han, C.; He, J.; Ni, Z.; Chen, W. Two-Dimensional Transition Metal Dichalcogenides: Interface and Defect Engineering. *Chem. Soc. Rev.* **2018**, *47*, 3100−3128.

(22) Liu, F.; Zhu, C.; You, L.; Liang, S. J.; Zheng, S.; Zhou, J.; Fu, Q.; He, Y.; Zeng, Q.; Fan, H. J.; Ang, L. K.; Wang, J.; Liu, Z. 2D Black Phosphorus/$SrTiO_3$-Based Programmable Photoconductive Switch. *Adv. Mater.* **2016**, *28*, 7768−7773.

(23) Li, Y.; Cai, C.; Gu, Y.; Cheng, W.; Xiong, W.; Zhao, C. Novel Electronic Properties of a New MoS_2/TiO_2 Heterostructure and Potential Applications in Solar Cells and Photocatalysis. *Appl. Surf. Sci.* **2017**, *414*, 34−40.

(24) Wazir, N.; Liu, R.; Ding, C.; Wang, X.; Ye, X.; Lingling, X.; Lu, T.; Wei, L.; Zou, B. Vertically Stacked $MoSe_2$/MoO_2 Nanolayered Photodetectors with Tunable Photoresponses. *ACS Appl. Nano Mater.* **2020**, *3*, 7543−7553.

(25) Pan, J.; Liu, Y.; Ou, W.; Li, S.; Li, H.; Wang, J.; Song, C.; Zheng, Y.; Li, C. The Photocatalytic Hydrogen Evolution Enhancement of the MoS_2 Lamellas Modified g-C_3N_4/$SrTiO_3$ Core-Shell Heterojunction. *Renewable Energy* **2020**, *161*, 340−349.

(26) Zhang, L.; Yin, J.; Wei, K.; Li, B.; Jiao, T.; Chen, Y.; Zhou, J.; Peng, Q. Fabrication of Hierarchical $SrTiO_3$@MoS_2 Heterostructure Nanofibers as Efficient and Low-Cost Electrocatalysts for Hydrogen-Evolution Reactions. *Nanotechnology* **2020**, *31*, 205604.

(27) Sarkar, S.; Goswami, S.; Trushin, M.; Saha, S.; Panahandeh-Fard, M.; Prakash, S.; Tan, S. J. R.; Scott, M.; Loh, K. P.; Adam, S.; Mathew, S.; Venkatesan, T. Polaronic Trions at the MoS_2/$SrTiO_3$ Interface. *Adv. Mater.* **2019**, *31*, 1903569.

(28) Trushin, M.; Sarkar, S.; Mathew, S.; Goswami, S.; Sahoo, P.; Wang, Y.; Yang, J.; Li, W.; MacManus-Driscoll, J. L.; Chhowalla, M.; Adam, S.; Venkatesan, T. Evidence of Rotational Fröhlich Coupling in Polaronic Trions. *Phys. Rev. Lett.* **2020**, *125*, 086803.

(29) Zhang, Y.; Ji, Q.; Han, G.-F.; Ju, J.; Shi, J.; Ma, D.; Sun, J.; Zhang, Y.; Li, M.; Lang, X.-Y.; Zhang, Y.; Liu, Z. Dendritic, Transferable, Strictly Monolayer MoS_2 Flakes Synthesized on $SrTiO_3$ Single Crystals for Efficient Electrocatalytic Applications. *ACS Nano* **2014**, *8*, 8617−8624.

(30) Zhang, Y.; Ji, Q.; Wen, J.; Li, J.; Li, C.; Shi, J.; Zhou, X.; Shi, K.; Chen, H.; Li, Y.; Deng, S.; Xu, N.; Liu, Z.; Zhang, Y. Monolayer MoS_2 Dendrites on a Symmetry-Disparate $SrTiO_3$(001) Substrate: Formation Mechanism and Interface Interaction. *Adv. Funct. Mater.* **2016**, *26*, 3299−3305.

(31) Yoon, W. Y.; Jin, H. J.; Jo, W. Reconfigurable Dipole-Induced Resistive Switching of MoS_2 Thin Layers on Nb:$SrTiO_3$. *ACS Appl. Mater. Interfaces* **2019**, *11*, 46344−46349.

(32) Yin, X.; Yang, M.; Tang, C. S.; Wang, Q.; Xu, L.; Wu, J.; Trevisanutto, P. E.; Zeng, S.; Chin, X. Y.; Asmara, T. C.; Feng, Y. P.; Ariando, A.; Chhowalla, M.; Wang, S. J.; Zhang, W.; Rusydi, A.; Wee, A. T. S. Modulation of New Excitons in Transition Metal Dichalcogenide-Perovskite Oxide System. *Adv. Sci.* **2019**, *6*, 1900446.

(33) Li, Y.; Qi, Z.; Liu, M.; Wang, Y.; Cheng, X.; Zhang, G.; Sheng, L. Photoluminescence of Monolayer MoS_2 on $LaAlO_3$ and $SrTiO_3$ Substrates. *Nanoscale* **2014**, *6*, 15248−15254.

(34) Chen, P.; Xu, W.; Gao, Y.; Warner, J. H.; Castell, M. R. Epitaxial Growth of Monolayer MoS_2 on $SrTiO_3$ Single Crystal

Substrates for Applications in Nanoelectronics. *Appl. Nano Mater.* **2018**, *1*, 6976−6988.

(35) Chen, P.; Xu, W.; Gao, Y.; Holdway, P.; Warner, J. H.; Castell, M. R. Thermal Degradation of Monolayer MoS_2 on $SrTiO_3$ Supports. *J. Phys. Chem. C* **2019**, *123*, 3876−3885.

(36) Goodman, A. J.; Lien, D. H.; Ahn, G. H.; Spiegel, L. L.; Amani, M.; Willard, A. P.; Javey, A.; Tisdale, W. A. Substrate-Dependent Exciton Diffusion and Annihilation in Chemically Treated MoS_2 and WS_2. *J. Phys. Chem. C* **2020**, *124*, 12175−12184.

(37) Li, X.; Zhang, S.; Chen, S.; Zhang, X.; Gao, J.; Zhang, Y. W.; Zhao, J.; Shen, X.; Yu, R.; Yang, Y.; He, L.; Nie, J.; Xiong, C.; Dou, R. Mo Concentration Controls the Morphological Transitions from Dendritic to Semicompact, and to Compact Growth of Monolayer Crystalline MoS_2 on Various Substrates. *ACS Appl. Mater. Interfaces* **2019**, *11*, 42751−42759.

(38) Bano, A.; Gaur, N. K. Interfacial Coupling Effect on Electron Transport in $MoS_2/SrTiO_3$ Heterostructure: An *ab-initio* Study. *Sci. Rep.* **2018**, *8*, 714.

(39) Bano, A.; Gaur, N. K. Effect of SrO Termination on Electron Transport of $MoS_2/SrTiO_3$ Heterostructure: A DFT Approach. *Appl. Surf. Sci.* **2019**, *487*, 1403−1408.

(40) Gaur, A.; Agarwal, T.; Asselberghs, I.; Radu, I.; Heyns, M.; Lin, D. A MOS Capacitor Model for Ultra-Thin 2D Semiconductors: The Impact of Interface Defects and Channel Resistance. *2D Mater.* **2020**, *7*, 035018.

(41) Pai, Y.-Y.; Tylan-Tyler, A.; Irvin, P.; Levy, J. Physics of $SrTiO_3$-Based Heterostructures and Nanostructures: A Review. *Rep. Prog. Phys.* **2018**, *81*, 036503.

(42) Christensen, D. V.; Trier, F.; Niu, W.; Gan, Y.; Zhang, Y.; Jespersen, T. S.; Chen, Y.; Pryds, N. Stimulating Oxide Heterostructures: A Review on Controlling $SrTiO_3$-Based Heterointerfaces with External Stimuli. *Adv. Mater. Interfaces* **2019**, *6*, 1900772.

(43) Biswas, A.; Rossen, P. B.; Yang, C. H.; Siemons, W.; Jung, M. H.; Yang, I. K.; Ramesh, R.; Jeong, Y. H. Universal Ti-Rich Termination of Atomically Flat $SrTiO_3$ (001), (110), and (111) Surfaces. *Appl. Phys. Lett.* **2011**, *98*, 051904.

(44) Chang, J.; Park, Y.-S.; Kim, S.-K. Atomically Flat Single-Terminated $SrTiO_3$ (111) Surface. *Appl. Phys. Lett.* **2008**, *92*, 152910.

(45) Chen, F.; Su, W. The Effect of the Experimental Parameters on the Growth of MoS_2 Flakes. *CrystEngComm* **2018**, *20*, 4823−4830.

(46) Shi, J.; Yang, Y.; Zhang, Y.; Ma, D.; Wei, W.; Ji, Q.; Zhang, Y.; Song, X.; Gao, T.; Li, C.; Bao, X.; Liu, Z.; Fu, Q.; Zhang, Y. Monolayer MoS_2 Growth on Au Foils and On-Site Domain Boundary Imaging. *Adv. Funct. Mater.* **2015**, *25*, 842−849.

(47) Liu, H.; Li, Y.; Xiang, M.; Zeng, H.; Shao, X. Single-Layered MoS_2 Directly Grown on Rutile TiO_2(110) for Enhanced Interfacial Charge Transfer. *ACS Nano* **2019**, *13*, 6083−6089.

(48) Lenser, C.; Koehl, A.; Slipukhina, I.; Du, H.; Patt, M.; Feyer, V.; Schneider, C. M.; Lezaic, M.; Waser, R.; Dittmann, R. Formation and Movement of Cationic Defects during Forming and Resistive Switching in $SrTiO_3$ Thin Film Devices. *Adv. Funct. Mater.* **2015**, *25* (40), 6360−6368.

(49) Szot, K.; Speier, W.; Breuer, U.; Meyer, R.; Szade, J.; Waser, R. Formation of Micro-Crystals on the (100) Surface of $SrTiO_3$ at Elevated Temperatures. *Surf. Sci.* **2000**, *460*, 112−128.

(50) Liu, H.; Zhu, D.; Shi, H.; Shao, X. Fabrication of a Contamination-Free Interface between Graphene and TiO_2 Single Crystals. *ACS Omega* **2016**, *1*, 168−176.

(51) Zheng, X.; Gerber, E.; Park, J.; Werder, D.; Kigner, O.; Kim, E. A.; Xie, S.; Schlom, D. G. Utilizing Complex Oxide Substrates to Control Carrier Concentration in Large-Area Monolayer MoS_2 Films. *Appl. Phys. Lett.* **2021**, *118*, 093103.

(52) Curcio, A.; Wang, J.; Wang, Z.; Zhang, Z.; Belotti, A.; Pepe, S.; Effat, M. B.; Shao, Z.; Lim, J.; Ciucci, F. Unlocking the Potential of Mechanochemical Coupling: Boosting the Oxygen Evolution Reaction by Mating Proton Acceptors with Electron Donors. *Adv. Funct. Mater.* **2021**, *31*, 2008077.

(53) Kuc, A.; Zibouche, N.; Heine, T. Influence of Quantum Confinement on the Electronic Structure of the Transition Metal Sulfide TS_2. *Phys. Rev. B: Condens. Matter Mater. Phys.* **2011**, *83*, 245213.

(54) Wu, H.; Kang, Z.; Zhang, Z.; Zhang, Z.; Si, H.; Liao, Q.; Zhang, S.; Wu, J.; Zhang, X.; Zhang, Y. Interfacial Charge Behavior Modulation in Perovskite Quantum Dot-Monolayer MoS_2 0D-2D Mixed-Dimensional van der Waals Heterostructures. *Adv. Funct. Mater.* **2018**, *28*, 1802015.